ADVANCED MATERIALS
www.advmat.de

Liquid-Flowing Graphene Chip-Based High-Resolution Electron Microscopy

*Kunmo Koo, Jungjae Park, Sanghyeon Ji, Saltanat Toleukhanova, and Jong Min Yuk**

The recent advances in liquid-phase transmission electron microscopy represent tremendous potential in many different fields and exciting new opportunities. However, achieving both high-resolution imaging and operando capabilities remain a significant challenge. This work suggests a novel in situ imaging platform of liquid-flowing graphene chip TEM (LFGC-TEM) equipped with graphene viewing windows and a liquid exchange system. The LFGCs are robust under high-pressure gradients and rapid liquid circulation in ranges covering the experimental conditions accessible with conventional thick SiN_x chips. LFGC-TEM provides atomic resolution for colloidal nanoparticles and molecular-level information limits for unstained wet biomolecules and cells that are comparable to the resolutions achievable with solid-phase and cryogenic TEM, respectively. This imaging platform can provide an opportunity for live imaging of biological phenomena that is not yet achieved using any current methods.

Liquid-phase transmission electron microscopy (LP-TEM) has emerged as a promising platform[1–4] to directly reveal a wide range of physical,[5–7] chemical,[8–11] and biological[12,13] phenomena that take place in liquids on the nanoscale. LP-TEM requires environmental cells containing a hermetically sealed reservoir and a viewing window fabricated from SiN_x.[3,8,9] Although such liquid cells can stably maintain intact liquid samples under high-vacuum TEM conditions, both the spatial information and signal-to-noise ratio (SNR) for TEM imaging are degraded by the relatively thick (15 to 50 nm) and high-atomic-number (Z) windows.[14,15] Moreover, bulging of the windows leads to a thicker liquid layer than initially intended.[16]

As an alternative window, graphene, a single-layer sheet of carbon atoms (Z = 6), has been proposed.[4,7,17] Since graphene has an intrinsically high Young's modulus (≈1 TPa), membrane bulging could be suppressed,[18] allowing for the maintenance of a thin liquid layer within graphene liquid cells (GLCs). As a result, GLCs have provided atomic resolution and high contrast for a broad range of materials, including light elements and organic molecules. Moreover, due to the impermeability of graphene to most molecules,[19] any aqueous or organic solution can be stably trapped without leakage during prolonged TEM observation. Additionally, graphene inherently has a high electrical and thermal conductivity, as well as radical scavenging properties,[20] and thus GLCs alleviate charging,[21] heating, and radiation damage to the sample under the electron beam.[22,23]

However, GLCs have pocket- or well-type cells hermetically sealed by Van der Waals interactions of graphene sheets. This fully confined structure has limited their application to electron-beam-induced processes, such as mineral precipitation,[24] growth and etching of colloidal particles,[4,11,25] and chemical lithiation of electrode materials.[26] The external stimuli required to mimic realistic reactions, such as reactive liquid injection, heating, and biasing current or voltage, could be implemented by the development of a graphene-based environmental cell system.[27] A transitional-type graphene-based flow cell has recently been implemented to enhance the spatial resolution by replacing the single-side of SiN_x window at the monolithic channel-type SiN_x liquid cell.[28] Nevertheless, the versatile structures are still required to improve the imaging performance and extend to Operando imaging with the adoption of external stimuli.

Here, we systematically designed graphene-windowed environmental cells capable of thin liquid layer formation and liquid injection (**Figure 1**). The liquid-flowing graphene chips (LFGCs) consist of a large top chip and a small bottom chip that fit into a commercial liquid-flowing TEM holder (Figure 1a). Each chip is fabricated by microelectromechanical system (MEMS) process on a 4-inch Si wafer, including depositing an SiN_x membrane, perforating the membrane with a holey pattern, and transferring few-layered graphene onto the holey-patterned SiN_x membrane (Figures S1–S5 and Section S1, Supporting Information). The thick SiN_x membrane and graphene serve as a bulging-resistive support and viewing window, respectively. The fabricated top and bottom chips can be assembled in the liquid-flowing TEM holder equipped with a liquid injection system (Figure 1b), where liquid flows through a channel opened by spacers on the bottom chip (Figure 1c). We demonstrate the physical properties of the implemented LFGCs under harsh conditions to confirm their structural stability during LP-TEM experiments. Furthermore, using liquid-flowing graphene chip TEM (LFGC-TEM), an enhanced contrast and resolution limit were obtained with several wet samples, such as polystyrene (PS) beads, liposomes, *Escherichia coli* bacteria, and colloidal gold nanoparticles (Au NPs), under liquid flowing conditions.

Dr. K. Koo, J. Park, S. Ji, S. Toleukhanova, Prof. J. M. Yuk
Department of Materials Science and Engineering
Korea Advanced Institute of Science and Technology (KAIST)
291 Daehak-ro, Yuseong-gu, Daejeon 34141, Republic of Korea
E-mail: jongmin.yuk@kaist.ac.kr

The ORCID identification number(s) for the author(s) of this article can be found under https://doi.org/10.1002/adma.202005468.

DOI: 10.1002/adma.202005468

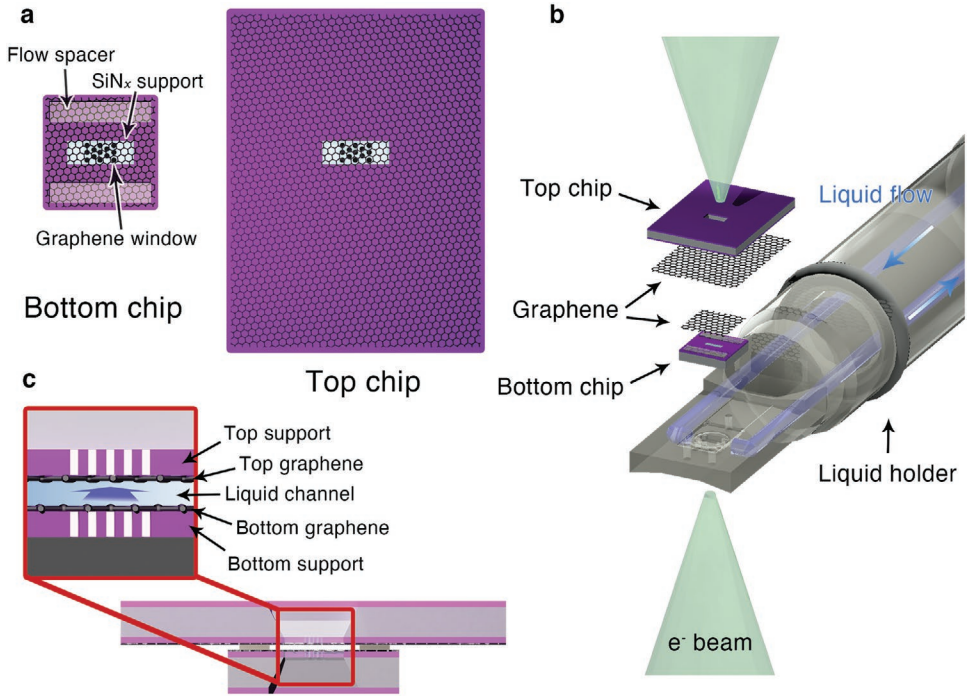

Figure 1. Schematics of LFGCs. a) Top view of separated LFGC. The LFGC consists of a large top chip and small bottom chip with spacers for a liquid flow channel. At the center of each chip, perforated SiN_x membranes are covered by graphene as a viewing window. b) Exploded schematic illustration of an LFGC loaded in a liquid-phase TEM holder. Liquid from outside the holder is infused through one side of the LFGC and effused to the other end. c) Cross-sectional view of an assembled LFGC. A liquid flow channel forms between the stacked top and bottom chips.

For the rational design of the LFGC system, variables that affect the overall spatial resolution in LP-TEM were analyzed. The spatial resolution (d_{TEM}) of LP-TEM is determined by the Scherzer resolution (d_{sch}), chromatic aberration-limited resolution (d_{cc}), electron dose-limited resolution (d_{SNR_phase}), and beam blur effect (d_{blur}):[14]

$$d_{TEM} = \sqrt{d_{sch}^2 + d_{CC}^2 + d_{SNR\_phase}^2 + d_{blur}^2} \quad (1)$$

Unlike in solid-phase electron microscopy, the LP-TEM resolution is affected by inelastic information loss from the liquid medium and sealing membrane. Specifically, the thickness and composition of both the membrane and liquid degrade the energy (d_{cc}) and angular (d_{blur}) distribution of the electron beam and restrict the overall resolution. **Figure 2**a illustrates the theoretical spatial resolution according to Equation (1) Below a liquid thickness of 100 nm, the TEM resolution is governed by membrane effects. For instance, the spatial resolution in SiN_x-based chips is restricted by the membrane-limited resolution even under the high-dose conditions applicable to the atomic-scale imaging of solid samples.[14] At the same liquid thickness, on the other hand, the electron dose is the dominant factor for determining spatial resolution in LFGCs because graphene significantly relieves both d_{cc} and d_{blur} (Figure S6 and Section S2, Supporting Information). As a result, the LFGC can provide an enhanced SNR and atomic-resolution imaging. In the assembled LFGCs, the graphene window regions have an almost 9 times higher measured brightness and more clearly resolved particle shapes than the SiN_x supporting region as proof of the relieved blur (Figure 2b and Figure S7, Supporting Information). However, above a liquid thickness of 100 nm, the spatial resolution is determined by the liquid thickness, which hampers atomic-scale imaging regardless of the membrane type. Thus, a liquid thickness below 100 nm is pivotal to achieving atomic-resolution imaging in LFGC-TEM.

The liquid thickness in an environmental cell is the sum of the spacer thickness and membrane-bulged thickness. The amount of bulge is determined by both the pressure difference between the inside and outside of the liquid cells and the stiffness of the membrane. One approach to controlling the deflection of the membrane is adjusting the internal pressure.[15] However, this requires complex methods that are incompatible with a continuous liquid flow configuration. Alternatively, the membrane deflection can be easily controlled by geometrical approaches, either by reducing the membrane width or by increasing its thickness. However, decreasing the membrane width leads to small viewing areas, leaving thickening of the membrane as an effective way to control the bulging. Thus, membrane deflection is calculated in terms of the membrane thickness. The calculated results show that a 50 nm thick SiN_x membrane has a maximum deflection of 467 nm under a 6000 Pa pressure gradient, which is equivalent to 5 µL min^{-1} of liquid flow (Figure 2c and Sections S3 and S4, Supporting Information). The deflection greatly decreases to 22 nm at an SiN_x thickness of 300 nm, whereas the decrement is minimized beyond this thickness because 300 nm is the saturation point of Young's modulus improvement of the thin film.[29] The simulations showed that the deflection of the viewing window is below 26 nm with a 300 nm thick perforated support regardless of the perforation pattern (Figure S9, Supporting Information).

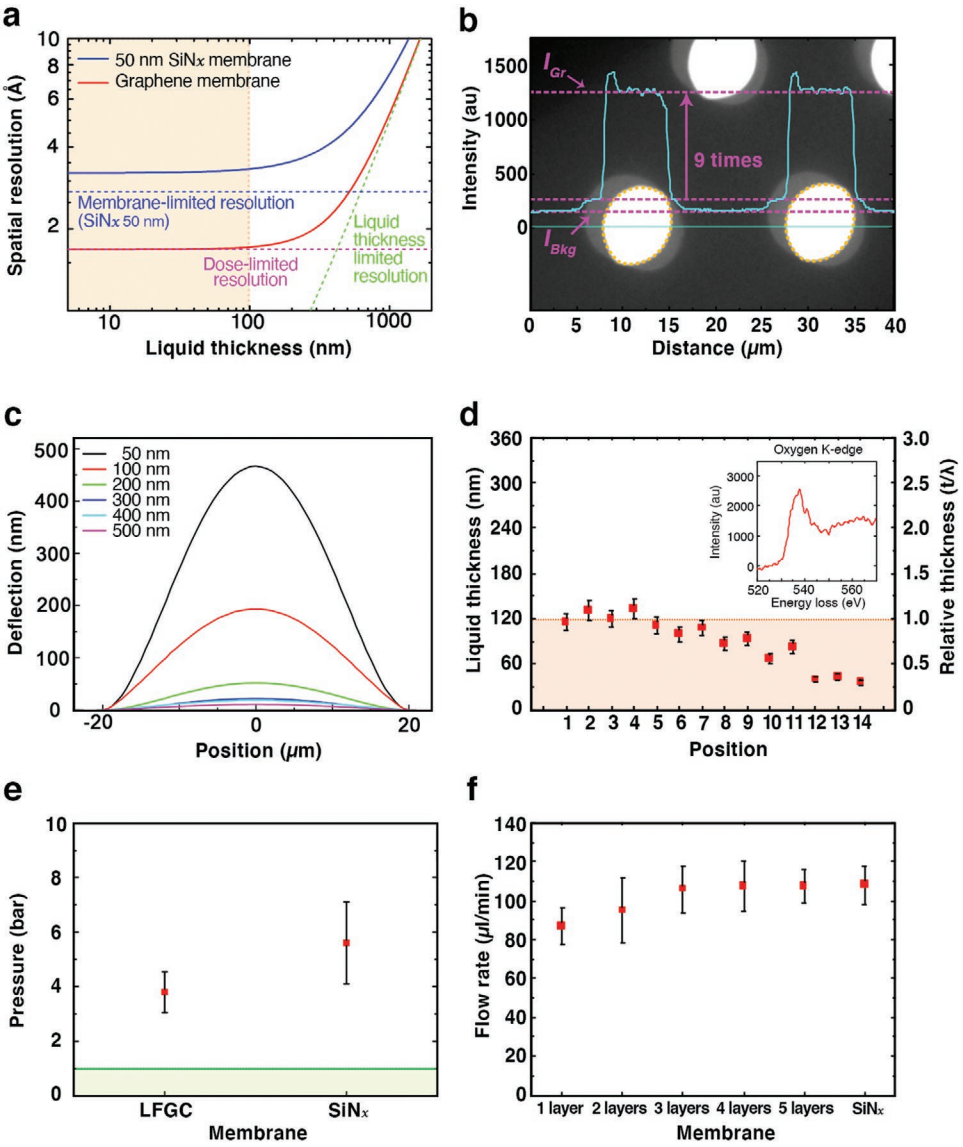

Figure 2. Physical properties of designed LFGCs. a) Simulated spatial resolution of liquid cells at a dose of 1×10^5 e^- $Å^{-2}$ including the membrane-limited (blue dashed), liquid thickness-limited (green dashed), and electron dose-limited (magenta dashed) resolutions. Solid blue and red lines indicate the LP-TEM resolutions composed of these three factors for SiN_x-based chips and LFGCs, respectively. The membrane-limited resolution in graphene is negligible. b) Electron micrograph and line profile of electron intensity showing the contrast between graphene and a 300 nm thick SiN_x membrane. c) Deflection of SiN_x membrane simulated with finite element analysis depending on thickness in the range from 50 to 500 nm under a 6000 Pa pressure gradient. d) Liquid thickness measured by the zero-loss EEL spectrum. The inset shows the oxygen core-loss spectrum measured with the LFGC. e) Pressure limit before rupture for the LFGCs and SiN_x chips. The green region indicates the pressure gradient imposed on the membrane during LP-TEM experiments. f) Liquid flow rate that the LFGCs and conventional SiN_x chips can withstand. The error bars in (d–f) indicate the standard deviation of 5–7 repeated experiments.

Therefore, the liquid thickness of approximately 100 nm necessary for atomic-resolution imaging is feasible with 30 nm thick spacers for the liquid flow channel.

The liquid thickness and internal morphology of LFGCs were calculated using electron energy loss spectroscopy (EELS) (Figure 2d and Figure S10, Supporting Information). The EEL spectra show that the liquid enclosed in LFGCs with 30 nm thick spacers has thicknesses ranging from 36 ± 3.6 to 132 ± 1.3 nm, which are in good agreement with the simulated values. Furthermore, due to the negligible inelastic scattering from the membrane and sufficiently thin liquid layer ($t/\lambda < 1$, where t is the sample thickness and λ is the mean free path of the inelastic scattered electrons), it is possible to acquire a sharp oxygen core-loss edge at approximately 530 eV and analyze the fine structure of oxygen in water (Figure 2d inset and Figure S11, Supporting Information).[17,30,31] Hence, the LFGCs also benefit chemical analyses using core-loss EELS more than SiN_x chips with a thick liquid layer ($t/\lambda > 2$–3).[16] Moreover, a thin liquid layer controlled by bulging-resistive supports has the additional advantage of dissipating gas bubbles generated

by the electron beam and retaining a constant liquid thickness because accumulated gas residues in the imaging area likely to glide freely out instead of trapping beneath deflected membranes (Figure S12, Supporting Information).[32]

In terms of stability during liquid cell experiments, the window must be impermeable to the solution and strong enough to prevent rupture and delamination caused by the pressure gradient and liquid stream. The impermeability of the LFGCs was examined with hydrogen gas. Hydrogen molecules were filled into the assembled LFGCs to a pressure of 1 bar, which was retained for more than 30 min with just one layer of graphene (Figure S13a, Supporting Information). Further, the pressure limit of the LFGCs was confirmed by a pressurized vessel test with argon gas. Based on stepwise increments in internal pressure, the LFGCs can withstand a pressure difference as high as 3–6 bar, while a 50 nm SiN_x cell can withstand 4–10 bar (Figure 2e). It was confirmed that the observed rupture initiated from the stacked graphene sheets rather than the SiN_x support (Figure S13b,c and Movie S1, Supporting Information). Although the maximum pressure that the graphene window can withstand is lower than that of the SiN_x window due to intrinsic defects or wrinkles,[33] the suspended graphene in the LFGCs is strong enough to seal liquid and gas under 1 bar, which is a commonly employed pressure for in situ liquid and gas experiments. The adhesive stability of the LFGCs against laminar force was also tested at liquid infusion rates from 0.1 to 120 μL min^{-1} (Figure 2f). A single layer of graphene can withstand a flow rate of up to 80 μL min^{-1}, and graphene with more than 3 layers maintains its integrity at the maximum flow rate.

To demonstrate the enhanced imaging properties of the proposed systems, an Au NP dispersed solution was constantly infused into the LFGCs and analyzed. An image of the Au NPs was acquired at a high resolution of 1.47 Å, which corresponds to the Au {220} planes (**Figure 3**a). This resolving power is remarkably enhanced compared with that of previous SiN_x-based liquid cells and comparable to that of solid-phase and veil-type GLC-TEM (Figure S14, Supporting Information).[4,24] Moreover, the LFGCs improve the SNR by ≈37% and beam blur by ≈ 52% compared with the use of 50 nm thick SiN_x chips (Figure 3b,c and Figure S15, Supporting Information).[13,15] During the constant infusion of the solution, the liquid diffuses into the gaps of the LFGC,[32] triggering consistent group movements of the NPs such as 3D displacement and rotation. The directional rolling behavior of the particles shows that their movement is affected by liquid diffusion relating with liquid infusion rate,[34] instead of stage drifts or lagging of particles by the liquid edge (Figure 3d,e and Movie S2, Supporting Information). In a static state, a small irregular movement caused by electron irradiation was observed. In contrast, the particles collectively moved with constant velocities of 1.34 ± 0.16 and 2.5 ± 0.21 nm s^{-1} at liquid infusion rates of 5 and 10 μL min^{-1}, respectively (Figure 3f and Figure S16, Supporting Information). Additionally, the diffusivity (D) of the particles increased from 0.99 to 2.5 nm^2 s^{-1} as the infusion rate increased. The mean square displacement (MSD) of the particles represents super-diffusion behavior following the power law (MSD $\approx 4Dt^{\alpha}$, $\alpha > 1$, where t is time) instead of linear diffusion, indicating Brownian motion (Figure 3g).[5–7]

Further, the corrosive etching of metal NPs was conducted by continuously flowing the etchant under a minimized electron flux. A high electron dose generates radiolysis products and accelerates the reaction kinetics to within a few minutes,[11,25] and thus the intermediate morphology could be missed. In the LFGCs, the intermediate shape evolution of the NPs can be observed at atomic resolution during etchant flow (Figure 3h and Movie S6, Supporting Information). Etching occurs preferentially at the corners of the NPs, following the nearest-neighbor broken-bond model.[11] After the corners flatten and relax to the {220} surface, dissolution occurs across the entire surface because of the similar coordination. Unlike accelerated etching by an electron beam, the repeated surface etching and flattening lead to the evolution of intermediate spherical NPs with irregular dimples, which would be missed by the electron-beam-induced etching process.

Unlike metal or inorganic nanocrystals, the mass thickness contrast of soft materials composed of light atoms is overwhelmed by a thick membrane and liquid.[13,21] Moreover, improving the resolution by increasing the electron dose is restricted because soft materials are easily degraded at high electron doses.[14] Therefore, the attainable resolution is limited to up to a few nanometers under an acceptable dose of 100 e^- $Å^{-2}$. Thus, to achieve high contrast and resolution with beam-sensitive materials, phase contrast should be employed. This phase contrast drastically decreases when the liquid becomes thicker than the single scattering mean free path of an electron, which is approximately 100–200 nm depending on the medium.[21,35] Due to the thin liquid layer employed in the LFGCs, beam-sensitive soft materials including PS beads, liposomes, and *E. coli* were directly observed without any treatments to enhance their contrast, such as staining or tagging with metal particles. During their imaging, the PS beads and liposomes maintained their spherical shapes without degradation, and the size of the liposome lipid bilayer was discriminated as 5 nm (**Figure 4**a,b). Further, the rod-shaped morphology of wet *E. coli* bacteria and their pili with a width of 5 nm were resolved (Figure 4c,d). The 5 nm imaging resolution reaches the maximum spatial resolution theoretically achievable using LFGCs at low-dose imaging conditions (Figure S6c, Supporting Information) and also corresponds to the resolution acquired from stained samples in SiN_x chips.[12]

Although the spatial resolution is restricted to a few nanometers in a single micrograph, detailed information on molecular structures could be restored by utilizing a computational algorithm, such as single-particle analysis for the structural determination of biomolecules. To reconstruct the structure at the molecular level, phase information should be transferred beyond the nanometer scale. Here, the phase information limit, which is the intersection of the transferred phase signal and the noise, governs the final resolution of the restored structures. To evaluate the phase information limit using the LFGCs, the contrast transfer function (CTF) of an image acquired from a 50 nm thick liquid was calculated (Figure 4e and Figure S17, Supporting Information). The cross-correlation of the acquired CTF with the simulated CTF demonstrated that the phase information is reliably transferred until 3.7 Å, where the crossover point with noise occurs (Figure 4f). This information limit is unprecedented in conventional environmental cells because the

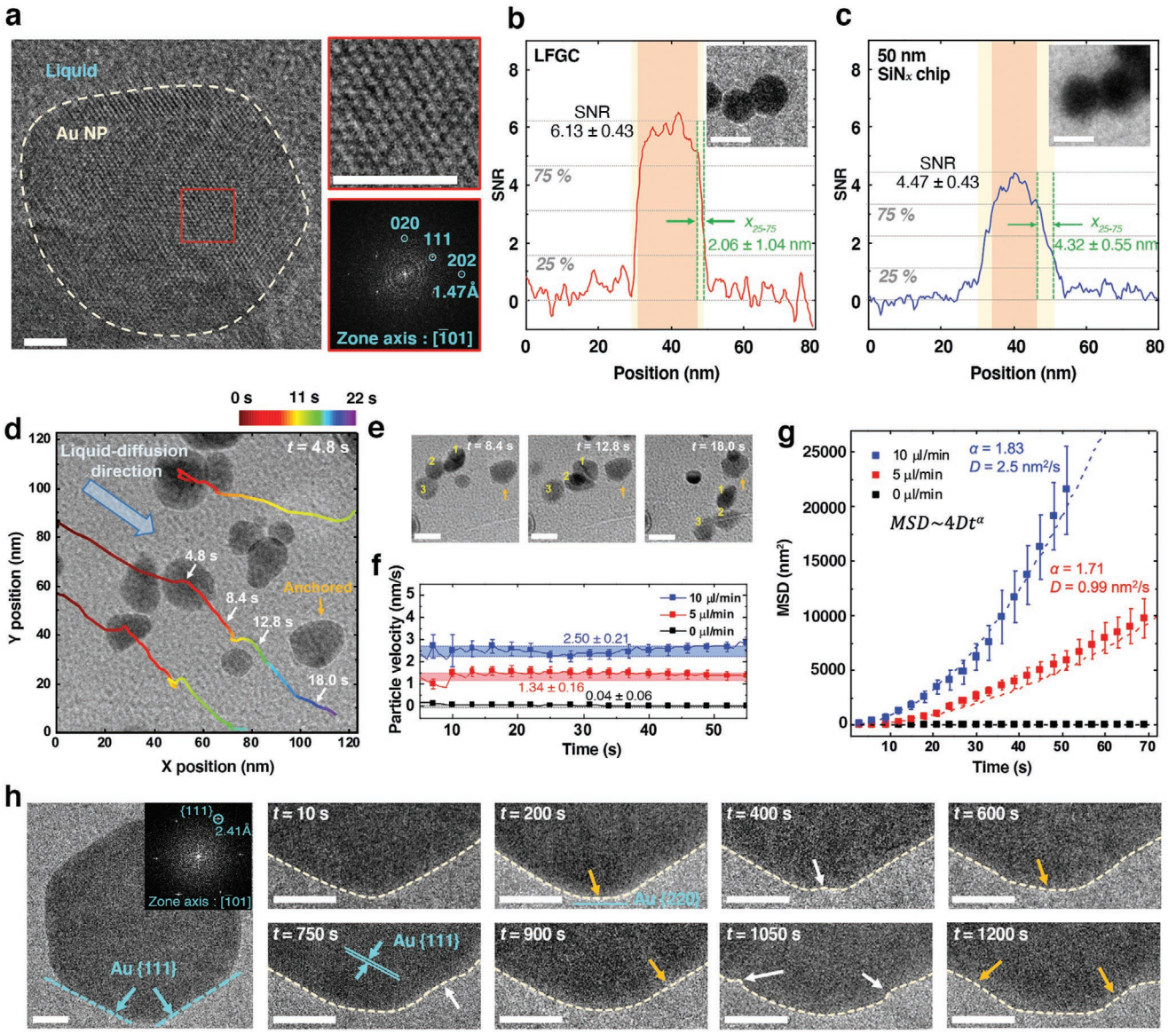

Figure 3. Atomic observation of Au NPs under liquid flow conditions. a) Atomic-resolution image of Au NPs suspended in a liquid environment (scale bar, 2 nm). The maximal lattice resolution reaches 1.47 Å. b,c) Line profiles of SNR in NPs observed in an b) LFGC and c) SiN_x chip. The 25–75% edge width of the maximal intensity (x_{25-75}) shows the beam blur effect. The insets are representative electron micrographs showing the beam blur effect in each liquid chip (scale bar, 20 nm). d) Group diffusion of NPs under continuous liquid circulation. The trajectories of particles are traced with time, and white and yellow arrows indicate moving and anchored particles on the graphene surface, respectively. e) Time-lapse images showing the particle movement of white arrows in (d) (scale bar, 20 nm). f) Velocity of particles depending on the liquid flow rate (Movies S3–S5, Supporting Information). g) MSDs of NPs at different flow rates. The dotted lines show the fitted MSDs following $4Dt^{\alpha}$. The error bars in (f,g) indicate standard deviations of 5–10 tracked particles. h) Oxidative etching of an icosahedral Au NP by etchant flowing (scale bar, 10 nm). The inset shows how each surface is bounded at {111} plane. The yellow and white arrows indicate the positions of flattening and etching, respectively. The electron doses or fluxes for image and movie were (a) 1100 e^{-} $Å^{-2}$, (b,c) 50 e^{-} $Å^{-2}$, (d) 670 e^{-} $Å^{-2}s$, and (h) 400 e^{-} $Å^{-2}s$.

noise from thick SiN_x windows and liquid layers disrupts the transfer of phase information on the nanometer scale. Besides, even if the liquid thickness is controllable below 100 nm, the existence of an SiN_x window restricts the overall phase information limit.[15] Moreover, this phase information limit is comparable to that acquired from vitreous ice by cryo-EM, which has a thickness of a few tens of nanometers.[35] This implies that atomic-resolution structural analysis of proteins in their native environment would be feasible with LFGCs by adopting the cryo-EM technique and a direct electron detector. Thus, LFGCs are a more appropriate liquid-cell platform for imaging soft materials at the molecular scale than conventional cells. Since the phase signal decays exponentially depending on the liquid thickness, large organisms requiring thick liquid layers should endure the loss of the phase signal, but natural contrast for specimens can be acquired without staining or tagging.[12]

In conclusion, we have presented LFGC-TEM as a novel imaging platform involving a graphene window and liquid

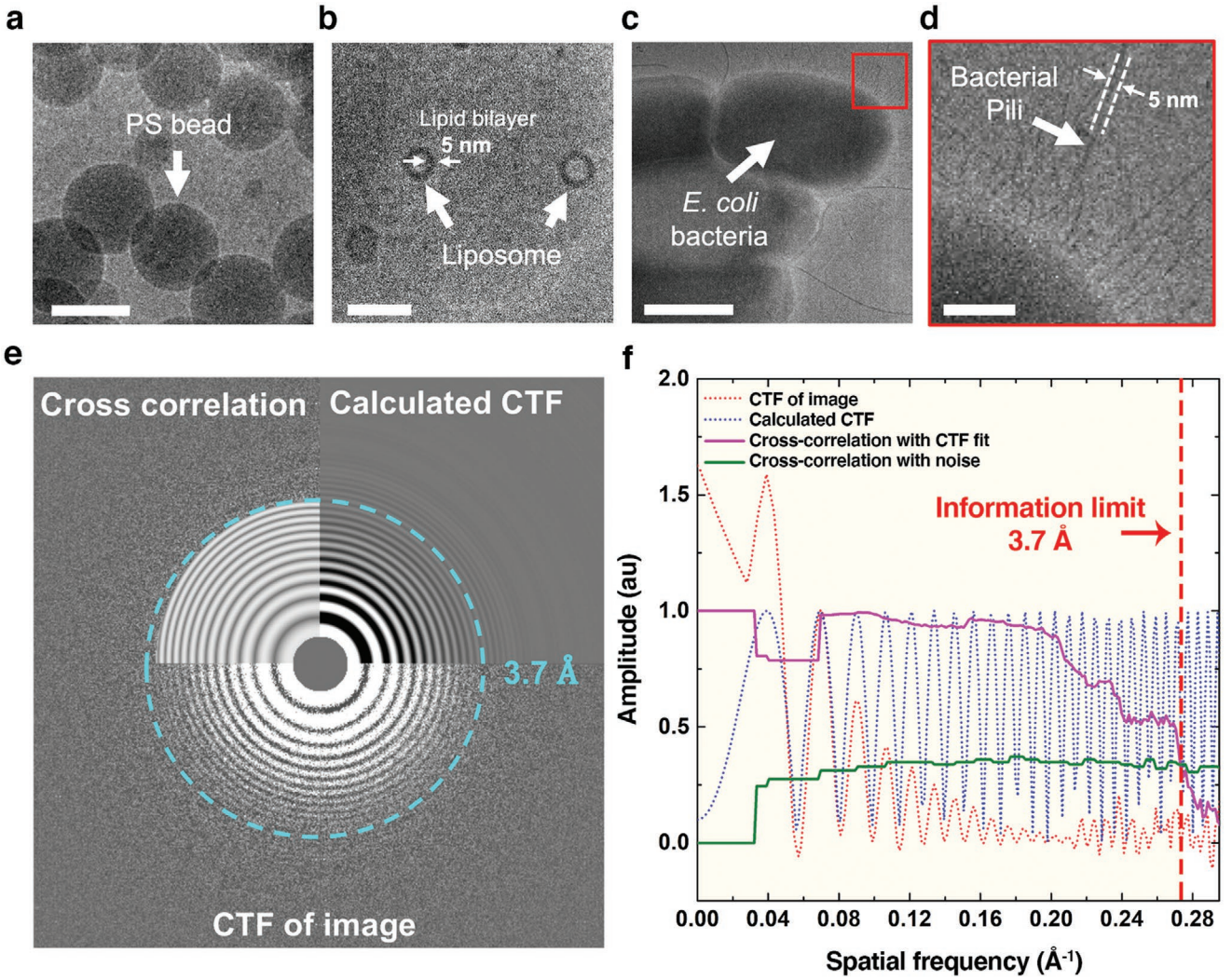

Figure 4. Imaging of electron-beam-sensitive materials at low electron doses. Electron micrographs of a) PS beads (scale bar, 50 nm), b) liposomes with a lipid bilayer (scale bar, 50 nm), and c) aggregated *E. coli* bacteria (scale bar, 1 µm). d) Bacterial pili with a thickness of 5 nm cropped from (c) (scale bar, 50 nm). e) CTF-corrected power spectrum acquired from 50 nm thick liquid in LFGCs. f) The measured information limit is 3.7 Å, where the crossover point occurs between cross-correlation with the simulated CTF and noise signal. The electron doses for image were (a) 100, (b) 30, (c) 20, and (e) 150 e^{-} $Å^{-2}$. Used spacer in the chips were (a,b) 50 nm and (c) 200 nm.

flow system. Although previous static GLCs have provided high-resolution imaging for in situ LP-TEM, their application is hampered by the low fabrication yields and small liquid volume of GLCs. The developed MEMS chips can be produced on a large scale and promote high-resolution LP-TEM experiments. Moreover, LFGCs can operate under more realistic conditions than small, static liquid cells, in which the composition of the trapped liquid continuously changes as the reaction proceeds and thus may cause misleading interpretations of reaction mechanisms. Especially, flushing of generated reactive radicals and prevention of their scavenging at graphene could enable high-dose electron imaging or prolonged TEM observations for biological specimens without their structural degradation.[20] In addition, LFGCs offer high-contrast imaging for wet biomolecules or cells without any markers such as tagging or staining. Thus, it is expected that single-molecule imaging for conformational dynamics, such as protein self-assembly, DNA hybridization, and virus infection, could be studied at the molecular level with LFGC-TEM.

The LFGCs can be made compatible with other external stimuli systems that conventional environmental cells offer, such as a biasing voltage or current or a heating and gas environment, and thus they can be modified into various environmental cells such as electrochemistry graphene chips (ECGCs), liquid-heating graphene chips (LHGCs), and gas-flowing graphene chips (GFGCs). Furthermore, for the potential application of LFGCs to the vast area of reactions regarding biology, energy science, and catalytic chemistry, the concept of separating the membrane and the viewing window can be modified with other atomic films as needed. For example, hexagonal boron nitride instead of graphene can be used for high-temperature experiments based on its high thermal and chemical stability. Transition-metal dichalcogenides, such as MoS_2 or WS_2, could also be used for the quantificational investigation of

organic compounds to avoid signal disturbance from the membrane elements.

Experimental Section

The detailed experimental process is available in the Supporting Information.

Supporting Information

Supporting Information is available from the Wiley Online Library or from the author.

Acknowledgements

K.K. and J.P. contributed equally to this work. This work was supported by the Samsung Research Funding & Incubation Center for Future Technology under Project Number SRFC-IT1701-15. The authors would like to thank Yun Chang Park at the National NanoFab Center (NNFC), Hye Jung Chang, Seung Min Kim, Min-Kyung Cho, and Junbeom Park at the Korea Institute of Science and Technology (KIST), and Young-Min Kim and Woo-Sung Jang at Sungkyunkwan University (SKKU) for their assistance with some of the EELS and TEM experiments.

Conflict of Interest

The authors declare no conflict of interest.

Keywords

atomic resolution imaging, biological imaging platforms, graphene liquid cells, liquid-phase transmission electron microscopy, operando electron microscopy

Received: August 12, 2020
Revised: October 24, 2020
Published online:

[1] F. M. Ross, *Science* **2015**, *18*, 350.
[2] J. J. De Yoreo, N. A. J. M. Sommerdijk, *Nat. Rev. Mater.* **2016**, *1*, 16035.
[3] N. De Jonge, F. M. Ross, *Nat. Nanotechnol.* **2011**, *6*, 695.
[4] J. M. Yuk, J. Park, P. Ercius, K. Kim, D. J. Hellebusch, M. F. Crommie, J. Y. Lee, A. Zettl, A. P. Alivisatos, *Science* **2012**, *336*, 61.
[5] H. Zheng, S. A. Claridge, A. M. Minor, A. P. Alivisatos, U. Dahmen, *Nano Lett.* **2009**, *9*, 2460.
[6] A. Verch, M. Pfaff, N. De Jonge, *Langmuir* **2015**, *31*, 6956.
[7] Q. Chen, J. M. Smith, J. Park, K. Kim, D. Ho, H. I. Rasool, A. Zettl, A. P. Alivisatos, *Nano Lett.* **2013**, *13*, 4556.
[8] M. J. Williamson, R. M. Tromp, P. M. Vereecken, R. Hull, F. M. Ross, *Nat. Mater.* **2003**, *2*, 532.
[9] H. Zheng, R. K. Smith, Y. W. Jun, C. Kisielowski, U. Dahmen, A. Paul Alivisatos, *Science* **2009**, *324*, 1309.
[10] J. Wu, W. Gao, H. Yang, J. M. Zuo, *ACS Nano* **2017**, *11*, 1696.
[11] X. Ye, M. R. Jones, L. B. Frechette, Q. Chen, A. S. Powers, P. Ercius, G. Dunn, G. M. Rotskoff, S. C. Nguyen, V. P. Adiga, A. Zettl, E. Rabani, P. L. Geissler, A. P. Alivisatos, *Science* **2016**, *354*, 874.
[12] E. Kennedy, E. M. Nelson, T. Tanaka, J. Damiano, G. Timp, *ACS Nano* **2016**, *10*, 2669.
[13] N. De Jonge, D. B. Peckys, G. J. Kremers, D. W. Piston, *Proc. Natl. Acad. Sci. USA* **2009**, *106*, 2159.
[14] N. de Jonge, L. Houben, R. E. Dunin-Borkowski, F. M. Ross, *Nat. Rev. Mater.* **2019**, *4*, 61.
[15] S. Keskin, P. Kunnas, N. De Jonge, *Nano Lett.* **2019**, *19*, 4608.
[16] M. E. Holtz, Y. Yu, J. Gao, H. D. Abruña, D. A. Muller, *Microsc. Microanal.* **2013**, *19*, 1027.
[17] C. Wang, Q. Qiao, T. Shokuhfar, R. F. Klie, *Adv. Mater.* **2014**, *26*, 3410.
[18] S. P. Koenig, N. G. Boddeti, M. L. Dunn, J. S. Bunch, *Nat. Nanotechnol.* **2011**, *6*, 543.
[19] S. Hu, M. Lozada-Hidalgo, F. C. Wang, A. Mishchenko, F. Schedin, R. R. Nair, E. W. Hill, D. W. Boukhvalov, M. I. Katsnelson, R. A. W. Dryfe, I. V. Grigorieva, H. A. Wu, A. K. Geim, *Nature* **2014**, *516*, 227.
[20] H. Cho, M. R. Jones, S. C. Nguyen, M. R. Hauwiller, A. Zettl, A. P. Alivisatos, *Nano Lett.* **2017**, *17*, 414.
[21] C. J. Russo, L. A. Passmore, *Curr. Opin. Struct. Biol.* **2016**, *37*, 81.
[22] S. Keskin, N. de Jonge, *Nano Lett.* **2018**, *18*, 7435.
[23] K. Koo, K. S. Dae, Y. K. Hahn, J. M. Yuk, *Nano Lett.* **2020**, *20*, 4708.
[24] J. M. Yuk, Q. Zhou, J. Chang, P. Ercius, A. P. Alivisatos, A. Zettl, *ACS Nano* **2016**, *10*, 88.
[25] S. Y. Kim, K. S. Dae, K. Koo, D. Kim, J. Park, J. M. Yuk, *Phys. Status Solidi Appl. Mater. Sci.* **2019**, *216*, 1800949.
[26] H. K. Seo, Y. Hwa, J. H. Chang, J. Y. Park, J. S. Lee, J. Park, E. J. Cairns, J. M. Yuk, *Nano Lett.* **2020**, *20*, 2080.
[27] F. M. Ross, *Liquid Cell Electron Microscopy*, Cambridge University Press, Cambridge, UK **2016**.
[28] G. Dunn, V. P. Adiga, T. Pham, C. Bryant, J. Donez, J. N. Belling, B. Lafrance, J. A. Jackson, R. Barzegar, J. M. Yuk, S. Aloni, M. F. Crommie, A. Zettl, *ACS Nano* **2020**, *14*, 9637.
[29] K. B. Gavan, H. J. R. Westra, E. W. J. M. Van Der Drift, W. J. Venstra, H. S. J. Van Der Zant, *Appl. Phys. Lett.* **2009**, *94*, 233108.
[30] S. M. Ghodsi, S. Anand, R. Shahbazian-Yassar, T. Shokuhfar, C. M. Megaridis, *ACS Nano* **2019**, *13*, 4677.
[31] G. Algara-Siller, O. Lehtinen, F. C. Wang, R. R. Nair, U. Kaiser, H. A. Wu, A. K. Geim, I. V. Grigorieva, *Nature* **2015**, *519*, 443.
[32] J. T. Van Omme, H. Wu, H. Sun, A. F. Beker, M. Lemang, R. G. Spruit, S. P. Maddala, A. Rakowski, H. Friedrich, J. P. Patterson, H. H. Pérez Garza, *J. Mater. Chem. C* **2020**, *8*, 10781.
[33] L. Wang, C. M. Williams, M. S. H. Boutilier, P. R. Kidambi, R. Karnik, *Nano Lett.* **2017**, *17*, 3081.
[34] E. A. Ring, N. De Jonge, *Microsc. Microanal.* **2010**, *16*, 622.
[35] P. J. B. Koeck, A. Karshikoff, *J. Microsc.* **2015**, *259*, 197.